# Coexistence of static and dynamic magnetism in the Kitaev spin liquid material Cu<sub>2</sub>IrO<sub>3</sub>

Eric M. Kenney, <sup>1</sup> Carlo U. Segre, <sup>2</sup> William Lafargue-Dit-Hauret, <sup>3</sup> Oleg I. Lebedev, <sup>4</sup> Mykola Abramchuk, <sup>1</sup> Adam Berlie, <sup>5</sup> Stephen P. Cottrell, <sup>5</sup> Gediminas Simutis, <sup>6</sup> Faranak Bahrami, <sup>1</sup> Natalia E. Mordvinova, <sup>4</sup> Gilberto Fabbris, <sup>7</sup> Jessica. L. McChesney, <sup>7</sup> Daniel Haskel, <sup>7</sup> Xavier Rocquefelte, <sup>3</sup> Michael J. Graf, <sup>1</sup> and Fazel Tafti <sup>1</sup>.\*

<sup>1</sup> Department of Physics, Boston College, Chestnut Hill, Massachusetts 02467, USA

<sup>2</sup> Department of Physics & CSRRI, Illinois Institute of Technology, Chicago, Illinois 60616, USA

<sup>3</sup> Univ Rennes, CNRS, ISCR (Institut des Sciences Chimiques de Rennes) UMR 6226, F-35000 Rennes, France

<sup>4</sup> Laboratoire CRISMAT, ENSICAEN-CNRS UMR6508, 14050 Caen, France

<sup>5</sup> ISIS Neutron and Muon Source, Science and Technology Facilities Council, Rutherford Appleton Laboratory,

Didcot OX11 0QX, United Kingdom

<sup>6</sup>Laboratory for Muon Spin Spectroscopy, Paul Scherrer Institute, 5232 Villigen PSI, Switzerland
<sup>7</sup>Advanced Photon Source, Argonne National Laboratory, Argonne, Illinois 60439, USA



(Received 4 April 2019; revised manuscript received 28 June 2019; published 12 September 2019)

Searching for a Kitaev spin liquid phase motivated intense research on the honeycomb iridate materials. However, access to a spin liquid ground state has been hindered by magnetic ordering.  $Cu_2IrO_3$  is a new honeycomb iridate without thermodynamic signatures of a long-range order. Here, we use muon spin relaxation to uncover the magnetic ground state of  $Cu_2IrO_3$ . We find a two-component depolarization with slow- and fast-relaxation rates corresponding to distinct regions with dynamic and static magnetism coexisting in the material. X-ray absorption spectroscopy and first-principles calculations identify a mixed copper valence as the origin of this behavior. Our results suggest that a minority of  $Cu^{2+}$  ions nucleate regions of static magnetism, whereas the majority of  $Cu^{4-}$  on the honeycomb lattice give rise to a Kitaev spin liquid.

#### DOI: 10.1103/PhysRevB.100.094418

#### I. INTRODUCTION

Long-range magnetic order is the natural ground state of an interacting electron system. Magnetic frustration is capable of disrupting the order and establishing a highly entangled ground state with nonlocal excitations known as a quantum spin liquid [1]. Among various spin liquid proposals, the Kitaev model has unique appeal because it offers an exact solution to a simple Hamiltonian  $(H_{ij} = -\sum_{\gamma} K_{\gamma} S_i^{\gamma} S_j^{\gamma})$  of spin-1/2 particles with bond-dependent ferromagnetic coupling  $(K_{\nu})$  [2]. The index  $\gamma$  corresponds to three inequivalent bonds at 120° on a honeycomb lattice. Two alkali iridates, Li<sub>2</sub>IrO<sub>3</sub> and Na<sub>2</sub>IrO<sub>3</sub>, were the first proposed Kitaev materials based on their honeycomb lattice structures that accommodate  $Ir^{4+}$  ions with pseudospin-1/2 ( $J_{eff} = 1/2$ ) [3–8]. Despite satisfying the basic assumptions of a Kitaev model, both compounds exhibited antiferromagnetic ordering with sharp peaks in both DC magnetization and heat capacity at 15 K [6,9]. Further investigations on the honeycomb [10,11], the hyperhoneycomb [12,13], and the harmonic honeycomb [14] materials revealed the presence of a Heisenberg interaction (J)and a symmetric off-diagonal interaction ( $\Gamma$ ) in the modified Hamiltonian of Kitaev materials [15,16]:

$$\mathcal{H} = \sum_{\langle i,j\rangle\gamma\neq\alpha,\beta} \left[ -K_{\gamma} S_{i}^{\gamma} S_{j}^{\gamma} + J \mathbf{S}_{i} \cdot \mathbf{S}_{j} + \Gamma \left( S_{i}^{\alpha} S_{j}^{\beta} + S_{i}^{\beta} S_{j}^{\alpha} \right) \right]. \tag{1}$$

The search for a Kitaev material with a negligible Heisenberg interaction and without a long-range order has recently led to a new honeycomb copper iridate, Cu<sub>2</sub>IrO<sub>3</sub> [17]. Despite having a magnetic moment and a Curie-Weiss temperature similar to those of the alkali iridates, Cu<sub>2</sub>IrO<sub>3</sub> barely revealed a small peak in zero-field-cooled (ZFC) DC magnetization at 2 K and a broad hump in the heat capacity [17]. The lack of a long-range magnetic order has been attributed to a more ideal honeycomb geometry with Ir-Ir-Ir bond angles closer to 120° [17]. These results indicated short-range (spin-glasslike) correlations and suggested proximity to the Kitaev spin liquid phase. A spin liquid ground state is expected to exhibit dynamical local fields without long-range ordering. Here, we use muon spin relaxation ( $\mu$ SR) as a direct probe of local magnetic fields and provide compelling evidence for a Kitaev spin liquid phase in  $Cu_2IrO_3$ . Our  $\mu SR$  results reveal both dynamic and static local fields in distinct volumes of the same sample at 50 mK. The origin of such behavior is traced to a mixed valence of Cu<sup>+</sup>/Cu<sup>2+</sup> by x-ray absorption spectroscopy and first-principles calculations.

## II. METHODS

### A. Material synthesis and magnetic measurements

 $\text{Cu}_2\text{IrO}_3$  was synthesized using a topotactic cation exchange reaction according to  $\text{Na}_2\text{IrO}_3 + 2\text{CuCl} \rightarrow \text{Cu}_2\text{IrO}_3 + 2\text{NaCl}$  under mild conditions (350 °C and 16 h). Details of the synthesis are explained in Ref. [17]. A high quality

<sup>\*</sup>fazel.tafti@bc.edu

of samples was confirmed by scanning transmission electron microscopy (STEM) and powder x-ray diffraction.

## B. Magnetization and muon spin relaxation

Magnetic susceptibility was measured using a Quantum Design MPMS-3 by stabilizing at each temperature and measuring the DC moment. The small peak in magnetization is sensitive to temperature stability and ZFC conditions. The  $\mu$ SR measurements were performed at the ISIS Pulsed Neutron and Muon Source at the Rutherford Appleton Laboratories (UK) using the EMU and MuSR spectrometers with the samples inside a dilution refrigerator and a helium exchange cryostat, respectively. The powder sample was pressed into a disk of 8 mm in diameter and 1.9 mm in thickness and was wrapped in a 12.5- $\mu$ m-thin silver foil. Measurements in the EMU were performed on a silver mounting pedestal in a dilution fridge (50 mK < T < 4.5 K, along with data at 16.4 K). Due to the small sample area, measurements inside the dilution refrigerator were made in flypast mode [18] in order to reduce the signal from muons not landing in the sample. In this case, the background results from muons landing in the cryostat. Measurements in the MuSR spectrometer were performed with the same sample mounted on a silver mounting plate in a helium exchange cryostat (1.7 K < T < 20 K). In this case the background results from muons landing in the silver holder. The background signals for each spectrometer were fixed at the values determined from long-time asymmetry at low temperatures (40% of the total signal for EMU, 76% for MuSR), where the sample was strongly magnetic. The total asymmetry was fixed at the value determined from the initial asymmetry at high temperatures where the material had no fast-relaxing component. The sample contribution to the asymmetry is the difference between these two values. Data were fit using WIMDA software [19] and all fits had a  $\chi^2$  per degree of freedom of approximately 1.01. The fitting parameter  $\alpha$ , which quantifies the efficiency mismatch between front and back detectors [20], was determined by the application of a weak transverse magnetic field.

## C. X-ray absorption near edge spectroscopy (XANES)

XANES measurements were performed at the Materials Research Collaborative Access Team (MRCAT), Sector 10-BM beamline at the Advanced Photon Source (APS) of Argonne National Laboratory (ANL) [21]. Between 2 and 5 mg of  $A_2$ IrO<sub>3</sub> (A = Li, Na, Cu) as well as IrO<sub>2</sub> powders were thoroughly ground with boron nitride (BN) as a filler and PVDF (polyvinylidene fluoride) as a binder, pressed into a 5-mm-diameter pellet, and encapsulated in thin Kapton tape. Low-temperature measurements were taken in transmission mode using a liquid-nitrogen-cooled stage (Linkam Scientific) at the Ir L<sub>3</sub> edge and the Cu K edge. The XANES data were reduced using the ATHENA program and fitted to structural models using the ARTEMIS program, both of the IFEFFIT suite [22,23]. Ir data were fitted with a single Ir-O path using a range of 2–12  $\text{Å}^{-1}$  ( $dk = 4 \text{Å}^{-1}$ ) in k-space and 1–2 Å(dR = 0.2 Å) in R-space and a weighting factor of  $k^2$ . Cu data were fitted using the same ranges but with multiple weighting factors of k,  $k^2$ , and  $k^3$  [24]. Cu data were fitted with a single

Cu-O path as well as multiple Cu-O paths. Cu L-edge data were collected at room temperature in total electron yield mode at the IEX beamline 29-ID of the APS, ANL. The beamline resolution was 250 meV. The Ir  $L_{2,3}$ -edge data used to compute the isotropic branching ratio were collected at beamline 4-ID-D of the APS, ANL.

## D. Electron microscopy

Transmission electron microscopy (TEM) including electron diffraction and high angle annular dark field scanning TEM (HAADF-STEM), annular bright field scanning TEM (ABF-STEM), and electron energy loss spectroscopy (EELS) experiments were performed using an aberration double-corrected JEM ARM200F microscope operated at 200 kV and equipped with a Centurio energy-dispersive X-ray spectroscopy (EDX) detector, an Orius Gatan CCD camera, and a GIF Quantum spectrometer. TEM samples were prepared by grinding the materials in an agate mortar with ethanol and depositing the obtained suspension on a Ni-carbon holey grid.

#### E. Density functional theory

The geometric optimization of Cu<sub>2</sub>IrO<sub>3</sub>, Cu<sub>1.5</sub>Na<sub>0.5</sub>SnO<sub>3</sub>, and Cu<sub>1.5</sub>Li<sub>0.5</sub>SnO<sub>3</sub> were implemented in the pseudopotential VASP code [25] using a projected augmented wave (PAW) method and the Perdew-Burke-Ernzerhof (PBE) exchangecorrelation potential [26]. The Hubbard correction was implemented using the scheme of Dudarev et al. [27] with  $U_{\text{eff}} = 3$ eV for iridium 5d orbitals and 5 eV for copper 3d orbitals. The atomic positions were relaxed until forces were converged to 0.03 eV/Å. Crystal structures were visualized using the VESTA program [28]. Simulations of the spectroscopic data were implemented in the full potential WIEN2K code [29] using a linearized augmented plane wave approach and a PBE0 hybrid functional with on-site corrections to iridium 5d and copper 3d orbitals. The radius of muffin tin was selected to be 1.46, 1.48, 1.50, 2.00, 2.00, and 1.94 bohr for O, Li, Na, Ir, Sn, and Cu atoms and the basis size control parameter was  $RK_{\text{max}} = 6$ . Both structural relaxation and spectroscopic calculations were spin polarized and included spin-orbit coupling.

## III. RESULTS AND DISCUSSIONS

## A. Muon spin relaxation

In  $\mu$ SR, spin-polarized positive muons are implanted in the sample, and the time evolution of the muon spin polarization in the local magnetic field is traced upon accumulating several million muon decay events. In Fig. 1(a), we show four muon polarization spectra in the zero applied field (ZF) at 300, 16, 4.5, and 0.05 K. The background is subtracted as described in the Supplemental Materials [30]. The ZF spectra at all temperatures are described by

$$P(t) = G_{KT}(t)[(1-f)\exp(-\lambda_{slow}t) + f\exp(-\lambda_{fast}t)], (2)$$

where  $G_{\rm KT}(t)$  is the Gaussian Kubo-Toyabe function describing depolarization by quasistatic randomly oriented magnetic moments [20] according to  $G_{\rm KT}(t)=\frac{1}{3}+\frac{2}{3}(1-\Delta^2t^2)\exp(-\frac{1}{2}\Delta^2t^2)$ . The spectrum at 300 K was fit to

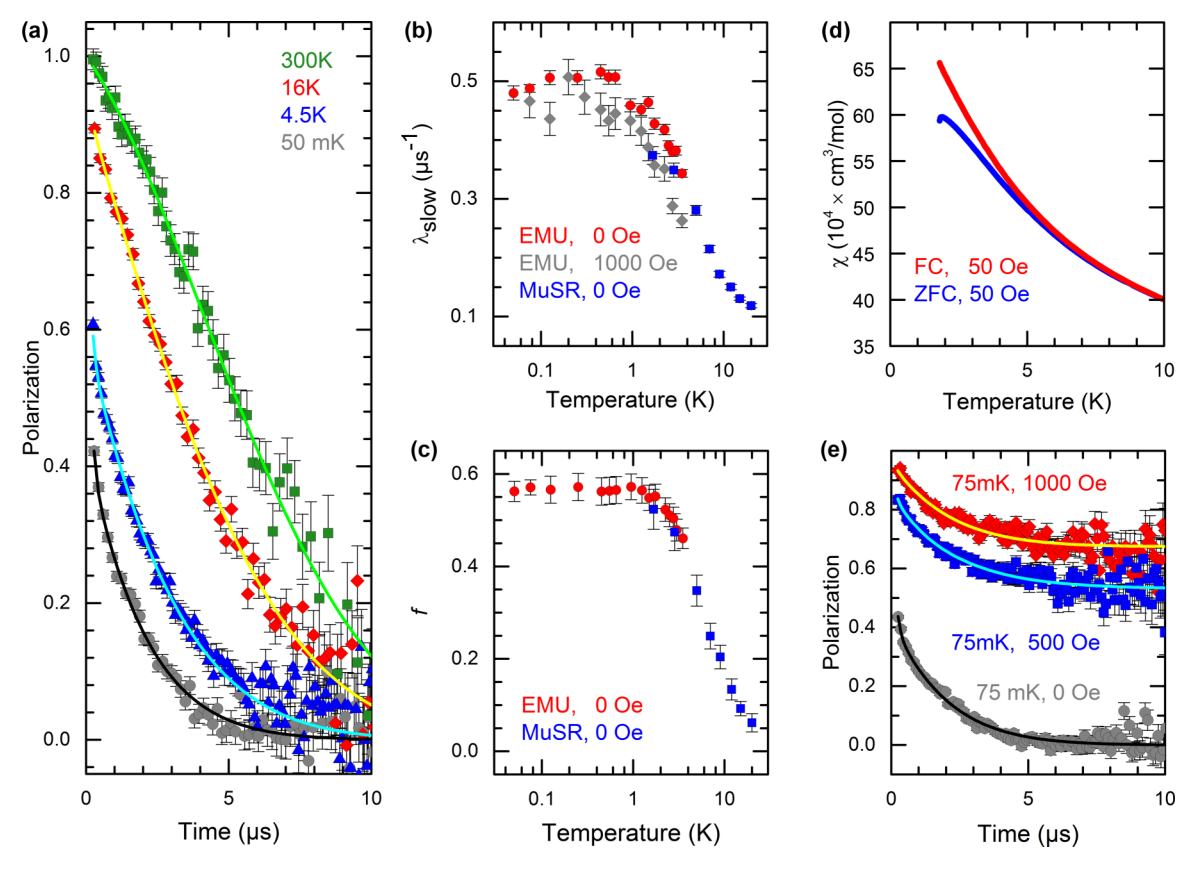


FIG. 1. (a) Representative zero field (ZF) spectra obtained at 300 K (green squares), 16 K (red diamonds), 4.5 K (blue triangles), and 0.05 K (gray circles). Continuous lines are fits to the data. (b) Temperature dependence of the slow-depolarization rate  $\lambda_{\rm slow}$  shows a plateau below 2 K at both ZF and LF of 1000 Oe with data extending over two decades of temperature from 20 to 0.05 K. (c) Temperature dependence of the fast-depolarization fraction f shows a plateau below 2 K. (d) DC magnetic susceptibility shows a small peak at 2 K and a splitting between field-cooled (FC) and zero-field-cooled (ZFC) at 10 K. (e)  $\mu$ SR spectra at 75 mK in several longitudinal fields show a persistent slow depolarization and a vanishing fast-depolarization component.

 $G_{\rm KT}$  (multiplied by a weak exponential decay) with  $\Delta = 0.11~\mu {\rm s}^{-1}$ , a typical rate for depolarization by Cu nuclear moments [31]. The inclusion of a  $G_{\rm KT}(t)$  does not affect the fits at lower temperatures, but for consistency we use Eq. (2) with a fixed  $\Delta$  to fit the data at all temperatures. The slow and fast exponential decays ( $\lambda_{\rm slow}$  and  $\lambda_{\rm fast}$ ) represent a two-component electronic spin contribution to the muon depolarization, and f is the fraction of the signal associated with the fast decay. We show below that  $\lambda_{\rm slow}$  and  $\lambda_{\rm fast}$  correspond to muons depolarizing in regions of dynamic and static magnetism, respectively.

In Fig. 1(a), the fast relaxation is primarily observed as a missing polarization at  $t < 0.2~\mu s$  which is outside the bandwidth of the pulsed muon facility. However, enough of the fast-relaxation tail leaks into the spectra in Fig. 1(a) to fit its contribution with a temperature-independent relaxation rate of  $\lambda_{\rm fast} = 9(3)~\mu s^{-1}$ . A pulsed muon source is particularly suitable to characterize the slow mode with the relaxation rate  $\lambda_{\rm slow} = 0.48(1)~\mu s^{-1}$  at 50 mK [Fig. 1(b)] which is 18 times slower than  $\lambda_{\rm fast}$ . Temperature dependencies of  $\lambda_{\rm slow}$  and f grow rapidly below 10 K. This onset of magnetism correlates with the temperature at which the field-cooled (FC) and zero-field-cooled (ZFC) susceptibility curves deviate [Fig. 1(d)]. With further decreasing temperature, both  $\lambda_{\rm slow}$  and f form

plateaus below  $T = 2 \,\mathrm{K}$  [Figs. 1(b) and 1(c)]. The onset of a plateau in f coincides with a small peak in the ZFC susceptibility [Fig. 1(d)], suggesting the presence of frozen spins in a fraction of the sample volume (see also transverse field data in the Supplemental Material, Fig. S2 [30]).

The field dependence of  $\mu$ SR can be used to probe the dynamics of the slow and fast modes. Figure 1(e) shows that the application of a 1000 Oe longitudinal field (LF) restores the missing polarization from the fast-relaxing muons, indicating the fast relaxation is caused by static local fields that are significantly less than 1000 Oe. In contrast, relaxation of the slow component persists in 1000 Oe LF and appears to be due to dynamic rather than static local fields. Because  $\lambda_{slow}$  $\ll \lambda_{\text{fast}}$ , if the local fields were static for slow-relaxing muons, we would expect the slow channel to also be suppressed by the 1000 Oe LF. Indeed, if the slow relaxation were caused by a static field, the magnitude of that field would be approximated by  $B_i = 2\pi \lambda_{\text{slow}}/\gamma_{\mu} = 37 \text{ Oe} \ll 1000 \text{ Oe}$   $(\gamma_{\mu}/2\pi = 135.5 \text{ MHz T}^{-1} \text{ is the muon gyromagnetic ratio}).$ The nearly unchanged relaxation rate and amplitude of the slow mode in 1000 Oe LF [Figs. 1(b) and 1(e)] demonstrate that it is caused by fluctuating local fields. Therefore, we ascribe  $\lambda_{fast}$  to muons depolarizing in static local fields and  $\lambda_{slow}$  to muons depolarizing via spin-liquid-like fluctuating local fields.

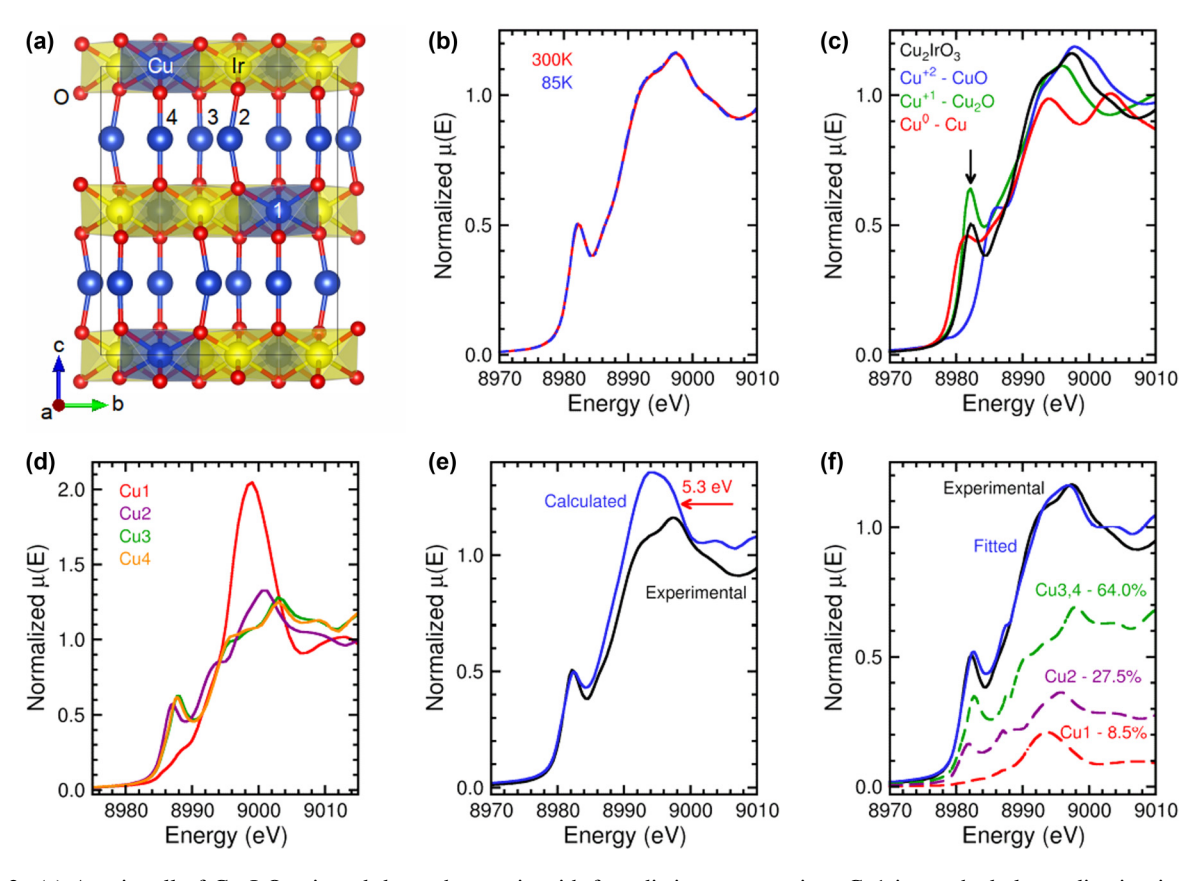


FIG. 2. (a) A unit cell of  $Cu_2IrO_3$  viewed down the a axis with four distinct copper sites. Cu1 in octahedral coordination is within the honeycomb layers, whereas  $Cu_2$ ,  $Cu_3$ , and  $Cu_4$  in dumbbell coordination are between the layers. (b) Normalized absorption coefficient plotted as a function of energy in  $Cu_2IrO_3$ . The  $\mu(E)$  curves are identical at 85 and 300 K. (c) Comparing  $\mu(E)$  between  $Cu_2IrO_3$  and three standard references. (d) Calculated absorption edge of  $Cu_3$  to  $Cu_4$  using the FEFF software. (e) Absorption spectrum of the  $Cu_3$  K edge is calculated by summing over the partial contributions from  $Cu_3$  to  $Cu_4$  with equal weights. The calculated signal is shifted by 5.3 eV to match the experimental data with acceptable but not perfect agreement. (f) A fit is made to the experimental XANES data where the weight of each partial contribution is a free parameter. The resulting weights for  $Cu_3$  are reported.  $Cu_3$  and  $Cu_4$  have the same weight. The fit errors are  $\pm 1\%$  for  $Cu_3$  and  $Cu_4$  for  $Cu_3$ , and  $Cu_4$ .

The LF experiment in Fig. 1(e) reveals important information about the distribution of the local static and dynamic fields in the material. With increasing LF from 0 to 1000 Oe, the fast depolarization disappears but the slow depolarization remains nearly unchanged. If the fluctuations were present throughout the sample volume, then a strong enough LF would decouple muons from the static local fields, leaving only magnetic fluctuations to depolarize muons. This would cause the fractional asymmetry associated with depolarization via fluctuations to increase with increasing LF. However, the fractional asymmetry does not increase [Fig. 1(e)], suggesting that some muons are stopped at sites with only a static field, while others are at sites with only fluctuating fields. Thus, static magnetism and dynamical fluctuations occupy distinct domains in the sample. The dynamic component is consistent with theoretical predictions of a Kitaev spin liquid in honeycomb iridates [4,15,32,33]. Next, we use spectroscopic techniques to reveal that a mixed valence of Cu is responsible for the static magnetic component in Cu<sub>2</sub>IrO<sub>3</sub>.

## B. X-ray absorption spectroscopy

Charge neutrality in  $Cu_2IrO_3$  dictates conjugate oxidation states of either  $Cu^+$  and  $Ir^{4+}$  or  $Cu^+/Cu^{2+}$  and  $Ir^{3+}$ .

 $\mathrm{Cu}^+$  [3 $d^{10}$ ] is nonmagnetic, whereas  $\mathrm{Cu}^{2+}$  [3 $d^9$ ] is magnetic with S=1/2.  $\mathrm{Ir}^{3+}$  [5 $d^6$ ] is nonmagnetic, whereas  $\mathrm{Ir}^{4+}$  [5 $d^5$ ] is magnetic with  $J_{\mathrm{eff}}=1/2$  due to one hole in the  $t_{2g}$  level [34]. Each unit cell of  $\mathrm{Cu}_2\mathrm{IrO}_3$  [Fig. 2(a)] contains three copper sites between the layers (Cu2, Cu3, and Cu4) in a dumbbell coordination and one copper site (Cu1) within the honeycomb layers in an octahedral coordination [17]. The typical coordination for  $\mathrm{Cu}^+$  is linear (dumbbells) and for  $\mathrm{Cu}^{2+}$  is square planar. An octahedral environment can accommodate both  $\mathrm{Cu}^+$  and  $\mathrm{Cu}^{2+}$ . Based on this argument we expect at least 75% of  $\mathrm{Cu}^+$  in  $\mathrm{Cu}_2\mathrm{IrO}_3$ .

XANES is a powerful tool to probe oxidation states. Our XANES data in Fig 2(b) show identical normalized absorption coefficients  $\mu(E)$  for the Cu K edge at 300 and 85 K confirming a temperature-independent ratio  $\mathrm{Cu^+/Cu^{2+}}$ . Figure 2(c) compares the Cu K-edge in  $\mathrm{Cu_2IrO_3}$  at room temperature to Cu, CuO, and  $\mathrm{Cu_2O}$ . The close similarity with  $\mathrm{Cu_2O}$  indicates a majority of  $\mathrm{Cu^+}$ . We calculated  $\mu(E)$  for the individual sites, Cu1 to Cu4, using the FEFF 8.40 code [24] based on the crystallographic data. The results in Fig. 2(d) show that Cu1 has a spectrum different from those of Cu2, Cu3, and Cu4 as expected from the coordination environments. Specifically, the edge for Cu1 is shifted to an energy higher than that of

the others, indicating a probable  $\mathrm{Cu}^{2+}$  state. Since all copper sites in  $\mathrm{Cu}_2\mathrm{IrO}_3$  have the same Wyckoff multiplicity [17], it is conceivable to reproduce the experimental curve by adding the four partial contributions in Fig. 2(d) with equal weight (25%). The resulting curve in Fig. 2(e) shows a mild disagreement with the experimental data. Specifically, the contribution from  $\mathrm{Cu}_1$  (nominally  $\mathrm{Cu}_2^{2+}$ ) appears to be overestimated. The experimental data can be more precisely fit to a weighted sum of partial  $\mu(E)$  contributions as reported in Fig. 2(f). According to this analysis, we estimate 8.5%  $\mathrm{Cu}^{2+}$  content, which means the honeycomb layers contain 1/3  $\mathrm{Cu}^{2+}$  ( $\frac{8.5\%}{25\%}$ ) and 2/3  $\mathrm{Cu}^+$ . This is only a rough estimate because we do not know the detailed structure of  $\mu(E)$  for  $\mathrm{Cu}^+$  in octahedral coordination.

The Cu<sup>2+</sup> content can also be estimated from the Cu Ledge XANES. Compared to the higher-energy Cu K edge, L-edge XANES involves electric-dipole transitions into empty Cu 3d states, resulting in dramatic differences between nominal  $3d^9$  and  $3d^{10}$  configurations. The main disadvantage is that accurate normalization of Cu L-edge data is not trivial. Figure 3(a) shows XANES data at the Cu L edge of Cu<sub>2</sub>IrO<sub>3</sub> compared to two references, namely, Cu<sub>2</sub>O (Cu<sup>+</sup>) and CuO (Cu<sup>2+</sup>) [35]. Absorption data were normalized by matching pre- and postedge regions to tabulated x-ray absorption cross sections as given by Cromer and Liberman [36]. The Cu<sup>2+</sup> ions resonate at 932 eV  $(L_3)$  and 952 eV  $(L_2)$ , while the Cu<sup>+</sup> ions resonate at 934 and 954 eV. The resonant enhancement of the absorption cross section ("white line") is much larger in CuO due in part to the larger density of empty 3d states. In  $Cu_2IrO_3$ , a double-peak structure is present at both  $L_2$  and  $L_3$ edges, indicating that both Cu<sup>2+</sup> and Cu<sup>+</sup> states are present. The Cu<sup>2+</sup> content was estimated from the ratio of white line intensities between Cu<sub>2</sub>IrO<sub>3</sub> and CuO samples independently evaluated at  $L_2$  and  $L_3$  edges. We obtained 6(2)% and 20(4)% for Cu  $L_2$ - and  $L_3$ -edge data, respectively. By averaging over the two L edges we arrive at a  $Cu^{2+}$  content of 13(5)%. These results are substantiated by self-consistent DFT calculations in the Supplemental Material, Fig. S4 [30], where the spectroscopic data are best reproduced using 12% Cu<sup>2+</sup> content.

To summarize,  $Cu^{2+}$  content is estimated 12% from DFT, 13% from Cu L-edge spectroscopy (1/2 of in-plane coppers), and 8.5% from Cu K-edge spectroscopy (1/3 of in-plane coppers). The spin-1/2  $Cu^{2+}$  ions can nucleate regions of static magnetism within each honeycomb layer giving rise to a fast depolarization of muons ( $\lambda_{fast}$ ). Outside these regions, the  $Cu^{+}/Ir^{4+}$  combination seems to form a spin liquid phase with dynamical local fields responsible for the slow depolarization of muons ( $\lambda_{slow}$ ). Note that all the iridium atoms are within the honeycomb layers. Based on the oxidation state of Cu and charge neutrality, approximately 80% of iridium atoms are in the  $Ir^{4+}$  state. This is confirmed by  $Ir L_3$ -edge spectroscopy in the Supplemental Material, Fig. S3 [30], which shows nearly identical  $L_3$  edges between  $Cu_2IrO_3$ ,  $Na_2IrO_3$ , and  $Li_2IrO_3$ .

The iridium L-edge spectroscopy also enables us to identify the  $J_{\text{eff}}$  states at the Fermi level in  $\text{Cu}_2\text{IrO}_3$  which are an important ingredient of the Kitaev model. The isotropic branching ratio (R), defined as the ratio of x-ray absorption cross sections at  $L_2$  and  $L_3$  edges involving spin-orbit split

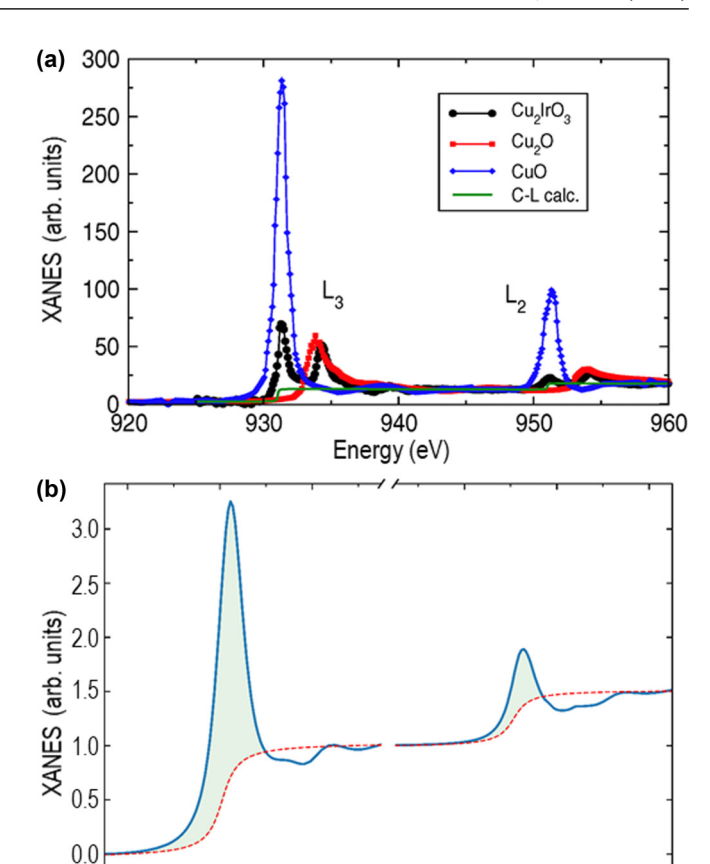


FIG. 3. (a) Cu  $L_2$ - and  $L_3$ -edge x-ray absorption data for Cu<sub>2</sub>IrO<sub>3</sub> together with Cu<sup>+</sup> and Cu<sup>2+</sup> reference spectra taken from the literature [35]. Data were normalized to Cromer-Liberman calculations of the single-atom x-ray absorption cross section [36]. The Cu<sup>2+</sup> content was estimated from white line intensity ratios in sample and references, averaged over L<sub>2</sub> and L<sub>3</sub> edges. (b) Iridium  $L_3$  (11.22 keV) and  $L_2$  (12.83 keV) edges are measured using XANES. The green area under each peak represents the absorption cross section with a branching ratio of  $R = I(L_3)/I(L_2) = 6$ .

Energy (keV)

12.82

12.84

12.86

11.20

11.22

11.24

 $2p_{3/2}$  and  $2p_{1/2}$  core levels  $[R = I(L_3)/I(L_2)]$ , is related to the expectation value of the angular part of the spin-orbit interaction in Ir 5d states, R = (2+r)/(1-r) with  $r = \langle \mathbf{L} \cdot \mathbf{S} \rangle / n_h$  $(n_h \text{ is the number of holes})$  [37,38]. The experimental R was calculated by integrating the resonant cross section at  $L_2$ and  $L_3$  edges after subtracting a step function broadened by the core-hole lifetime to emulate the single-atom absorption process. A R = 6.0(2) value was obtained by computing the ratio of white line intensities shown by the green shaded areas in Fig. 3(b). The strong deviation from the statistical value R=2 indicates unquenched spin-orbit interaction in the Ir 5d bands. Assuming  $n_h = 5$ , the experimental R yields  $\langle \mathbf{L} \cdot \mathbf{S} \rangle =$ 2.85(6) in units of  $\hbar^2$ . This is in excellent agreement with theoretical estimates of  $\langle \mathbf{L} \cdot \mathbf{S} \rangle = 3\hbar^2$  for a  $J_{\text{eff}} = 1/2$  ground state in Ir<sup>4+</sup> configuration (including contributions from four holes in  $e_g$ -like states), assuming an octahedral crystal field 10Dq = 3 eV and  $5d \text{ spin-orbit interaction } \xi_{5d} = 0.5 \text{ eV}$  [38]. The presence of  $J_{\text{eff}} = 1/2$  states at  $E_F$  is also confirmed by DFT calculations in the Supplemental Material, Fig. S7

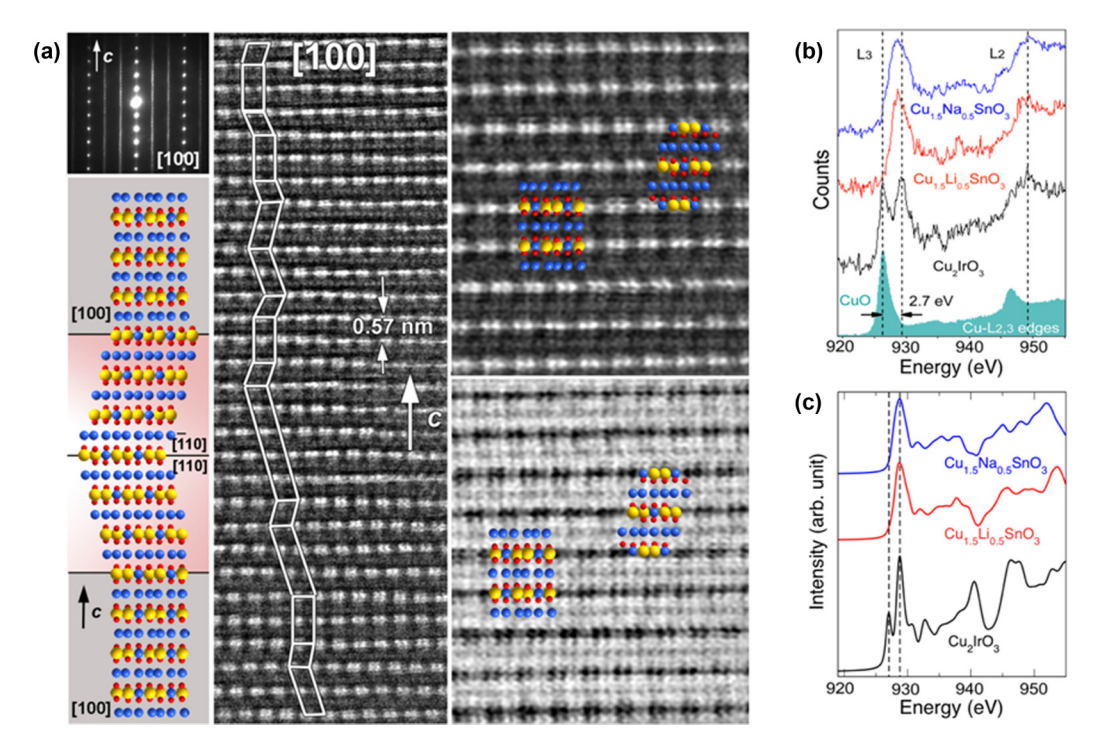


FIG. 4. (a) STEM is used to reveal perfect honeycomb ordering and twinned stacking disorder in  $Cu_2IrO_3$ . The top left image is an electron diffraction pattern along [100] where the streaking reveals stacking disorder along the c axis. The middle panel shows a HAADF-STEM image along [100] with a zigzag stacking that is modeled in the left inset as a twinning between [100], [110], and [ $\bar{1}$ 10] directions. Yellow, blue, and red circles represent Ir, Cu, and O atoms, respectively. The right top and bottom panels are magnified HAADF-STEM and ABF-STEM images, respectively. In each image, one unit cell along [100] and one unit cell along [ $\bar{1}$ 10] are modeled. Perfect honeycomb ordering is observed within each layer. (b) Experimental EELS spectra are compared between the stannates,  $Cu_{1.5}Li_{0.5}SnO_3$  and  $Cu_{1.5}Na_{0.5}SnO_3$ , and the iridate  $Cu_2IrO_3$ . Only one  $L_3$  peak is observed in the stannates corresponding to  $Cu^+$  (note the CuO reference).  $Cu_2IrO_3$  shows two  $L_3$  peaks corresponding to  $Cu^+$  and  $Cu^{2+}$ . (c) Self-consistent DFT calculations reproduce EELS spectra in agreement with the experiments. The calculations reveal one peak in stannates corresponding to  $Cu^+$  in dumbbell coordination but two peaks in  $Cu_2IrO_3$  due to mixed valence of copper (see Supplemental Material for details of DFT calculations [30]).

[30]. These results confirm the relavance of a Kitaev model to Cu<sub>2</sub>IrO<sub>3</sub> despite the mixed valence.

## C. Electron microscopy

The most fundamental ingredient of a Kitaev material, apart from spin-1/2 particles, is the honeycomb geometry. A direct image of the Cu<sub>2</sub>IrO<sub>3</sub> lattice obtained by TEM is presented in Fig. 4(a) (TEM). The middle panel is a HAADF-STEM image of a view down the [100] axis of a small crystallite. It reveals a zigzag stacking pattern along the c axis that is modeled in the left inset as a rotation (twinning) between adjacent layers with alternating [100], [110], and [110] orientations. A similar twinned stacking disorder, i.e.,  $\pm 60^{\circ}$  rotation between adjacent layers, is observed in related stannate materials, Cu<sub>1.5</sub>Li<sub>0.5</sub>SnO<sub>3</sub> and Cu<sub>1.5</sub>Na<sub>0.5</sub>SnO<sub>3</sub> with alkali/tin honeycomb layers [39]. In the right upper and lower insets of Fig. 4(a), unit cell models with [100] and [ $\bar{1}10$ ] orientations are overlaid on magnified views of the HAADF-STEM and ABF-STEM images, respectively. In both images, the layers exhibit a flawless pattern of Ir pairs separated by individual Cu atoms which is characteristic of honeycomb ordering [39]. Therefore, despite a twinned stacking disorder, each individual layer in Cu<sub>2</sub>IrO<sub>3</sub> has perfect honeycomb ordering without site mixing or vacancies.

TEM is also used for EELS with the data presented in Fig. 4(b). A comparison between the  $L_3$  edge in stannates and Cu<sub>2</sub>IrO<sub>3</sub> confirms that Cu<sub>2</sub>IrO<sub>3</sub> contains both Cu<sup>+</sup> and Cu<sup>2+</sup> whereas the stannates contain only Cu<sup>+</sup>. In the stannates, Cu atoms are restricted between the honeycomb layers in a dumbbell coordination [39]. Thus, all Cu<sup>2+</sup> in Cu<sub>2</sub>IrO<sub>3</sub> must be contained within the layers. Self-consistent DFT calculations in Fig. 4(c) reproduce the EELS spectra and confirm a single  $L_3$  peak in stannates but two distinct peaks in Cu<sub>2</sub>IrO<sub>3</sub>.

## IV. SUMMARY

To summarize,  $Cu_2IrO_3$  contains a majority/minority of  $Cu^+/Cu^{2+}$ . Seventy-five percent of Cu atoms are between the layers and in the +1 state. The remaining 25% are within the honeycomb layers, 1/3 to 1/2 of which are in the +2 state. Therefore, approximately 80% of Ir atoms are in the +4 state with  $J_{\rm eff}=1/2$ .  $\mu SR$  reveals two distinct magnetic environments (static and dynamic) in distinct volumes of the sample. This suggests that  $Cu^{2+}/Ir^{3+}$  ions segregate in regions of static magnetism, whereas the  $Cu^+/Ir^{4+}$  ions form regions of Kitaev spin liquid within the honeycomb layers. Muons could implant either in the static magnetic domains and exhibit fast depolarization or in the spin liquid domains and exhibit slow depolarization. We present data collapse

of magnetic susceptibility as a function of both temperature and field in the Supplemental Materials [30] consistent with recent theoretical and experimental studies of disordered spin liquid systems [40,41]. The coexistence of static and dynamic magnetism in Cu<sub>2</sub>IrO<sub>3</sub> highlights the robustness of a Kitaev spin liquid phase in the presence of magnetic disorder.

#### ACKNOWLEDGMENTS

We are grateful to Y. Ran, P. Blaha, and J. Kim for fruitful discussions. F.T., M.A., and F.B. acknowledge support from the National Science Foundation, Grant No. DMR–1708929.

MRCAT operations are supported by the Department of Energy and the MRCAT member institutions. Experiments at the ISIS Pulsed Neutron and Muon Source were supported by a beamtime allocation from the Science and Technology Facilities Council. O.I.L. acknowledges financial support from the "Agence Nationale de la Recherche" in the framework of the "Investissements d'avenir" program with the reference "ANR-11-EQPX-0020" for EELS data obtained using GIF Quantum. W.L.-D.-H. and X.R. thank access to the HPC resources of [TGCC/CINES/IDRIS] under allocation 2017-A0010907682 made by GENCI. Work at the APS was supported by the U.S. Department of Energy (DOE), Office of Science, under Contract No. DE-AC02-06CH11357.

- [1] L. Savary and L. Balents, Rep. Prog. Phys. 80, 016502 (2017).
- [2] A. Kitaev, Ann. Phys. (Amsterdam, Neth.) 321, 2 (2006).
- [3] Y. Singh and P. Gegenwart, Phys. Rev. B 82, 064412 (2010).
- [4] J. Chaloupka, G. Jackeli, and G. Khaliullin, Phys. Rev. Lett. 105, 027204 (2010).
- [5] Y. Singh, S. Manni, J. Reuther, T. Berlijn, R. Thomale, W. Ku, S. Trebst, and P. Gegenwart, Phys. Rev. Lett. 108, 127203 (2012).
- [6] S. K. Choi, R. Coldea, A. N. Kolmogorov, T. Lancaster, I. I. Mazin, S. J. Blundell, P. G. Radaelli, Y. Singh, P. Gegenwart, K. R. Choi, S.-W. Cheong, P. J. Baker, C. Stock, and J. Taylor, Phys. Rev. Lett. 108, 127204 (2012).
- [7] J. Chaloupka, G. Jackeli, and G. Khaliullin, Phys. Rev. Lett. 110, 097204 (2013).
- [8] M. Majumder, R. S. Manna, G. Simutis, J. C. Orain, T. Dey, F. Freund, A. Jesche, R. Khasanov, P. K. Biswas, E. Bykova, N. Dubrovinskaia, L. S. Dubrovinsky, R. Yadav, L. Hozoi, S. Nishimoto, A. A. Tsirlin, and P. Gegenwart, Phys. Rev. Lett. 120, 237202 (2018).
- [9] K. Mehlawat, A. Thamizhavel, and Y. Singh, Phys. Rev. B 95, 144406 (2017).
- [10] K. W. Plumb, J. P. Clancy, L. J. Sandilands, V. V. Shankar, Y. F. Hu, K. S. Burch, H.-Y. Kee, and Y.-J. Kim, Phys. Rev. B 90, 041112(R) (2014).
- [11] J. A. Sears, Y. Zhao, Z. Xu, J. W. Lynn, and Y.-J. Kim, Phys. Rev. B 95, 180411(R) (2017).
- [12] T. Takayama, A. Kato, R. Dinnebier, J. Nuss, H. Kono, L. S. I. Veiga, G. Fabbris, D. Haskel, and H. Takagi, Phys. Rev. Lett. 114, 077202 (2015).
- [13] L. S. I. Veiga, M. Etter, K. Glazyrin, F. Sun, C. A. Escanhoela, G. Fabbris, J. R.L. Mardegan, P. S. Malavi, Y. Deng, P. P. Stavropoulos, H. Y. Kee, W. G. Yang, M. van Veenendaal, J. S. Schilling, T. Takayama, H. Takagi, and D. Haskel, Phys. Rev. B 96, 140402(R) (2017).
- [14] K. A. Modic, T. E. Smidt, I. Kimchi, N. P. Breznay, A. Biffin, S. Choi, R. D. Johnson, R. Coldea, P. Watkins-Curry, G. T. McCandless, J. Y. Chan, F. Gandara, Z. Islam, A. Vishwanath, A. Shekhter, R. D. McDonald, and J. G. Analytis, Nat. Commun. 5, 4203 (2014).
- [15] J. G. Rau, Eric Kin-Ho Lee, and H.-Y. Kee, Phys. Rev. Lett. 112, 077204 (2014).
- [16] K. Hu, F. Wang, and J. Feng, Phys. Rev. Lett. 115, 167204 (2015).

- [17] M. Abramchuk, C. Ozsoy-Keskinbora, J. W. Krizan, K. R. Metz, D. C. Bell, and F. Tafti, J. Am. Chem. Soc. 139, 15371 (2017).
- [18] M. C. Lynch, S. P. Cottrell, P. J. C. King, and G. H. Eaton, Phys. B: Condensed Matter 326, 270 (2003).
- [19] F. L. Pratt, Phys. B (Amsterdam, Neth.) 289-290, 710 (2000).
- [20] A. Yaouanc and P. Dalmas de Réotier, Muon Spin Rotation, Relaxation, and Resonance: Applications to Condensed Matter, International Series of Monographs on Physics (Oxford University, Oxford, 2011).
- [21] A. J. Kropf, J. Katsoudas, S. Chattopadhyay, T. Shibata, E. A. Lang, V. N. Zyryanov, B. Ravel, K. McIvor, K. M. Kemner, K. G. Scheckel, S. R. Bare, J. Terry, S. D. Kelly, B. A. Bunker, and C. U. Segre, AIP Conf. Proc. 1234, 299 (2010).
- [22] M. Newville, J. Synchrotron Radiat. 8, 322 (2001).
- [23] B. Ravel and M. Newville, J. Synchrotron Radiat. 12, 537 (2005).
- [24] J. J. Rehr, J. J. Kas, M. P. Prange, A. P. Sorini, Y. Takimoto, and F. Vila, C. R. Phys. 10, 548 (2009).
- [25] G. Kresse and J. Furthmüller, Comput. Mater. Sci. 6, 15 (1996).
- [26] J. P. Perdew, K. Burke, and M. Ernzerhof, Phys. Rev. Lett. 77, 3865 (1996).
- [27] S. L. Dudarev, G. A. Botton, S. Y. Savrasov, C. J. Humphreys, and A. P. Sutton, Phys. Rev. B 57, 1505 (1998).
- [28] K. Momma and F. Izumi, J. Appl. Crystallogr. 44, 1272 (2011).
- [29] P. Blaha, K. Schwarz, G. Madsen, D. Kvasnicka, J. Luitz, R. Laskowski, F. Tran, and L. Marks, WIEN2K: An Augmented Plane Wave Plus Local Orbital Program for Calculating Crystal Properties, Karlheinz Schwarz, Technische Universität, Wien, Austria, 2018.
- [30] See Supplemental Material at http://link.aps.org/supplemental/ 10.1103/PhysRevB.100.094418 for analysis of the muon spin relaxation data collected in the helium-exchange cryostat, XANES data from L-edge of Ir for Cu<sub>2</sub>IrO<sub>3</sub> and three reference materials, DFT calculations, time-lapsed EELS spectra, ED patterns, elemental maps, PXRD analysis confirming high quality of the Cu<sub>2</sub>IrO<sub>3</sub> sample, and scaling analysis of the DC magnetization data.
- [31] G. M. Kalvius, O. Hartmann, A. Günther, A. Krimmel, A. Loidl, R. Wäppling, K. Sedlak, and R. Scheuermann, J. Phys.: Conf. Ser. 551, 012015 (2014).
- [32] Y. Yamaji, Y. Nomura, M. Kurita, R. Arita, and M. Imada, Phys. Rev. Lett. 113, 107201 (2014).

- [33] K. Slagle, W. Choi, L. E. Chern, and Y. B. Kim, Phys. Rev. B 97, 115159 (2018).
- [34] B. J. Kim, H. Jin, S. J. Moon, J.-Y. Kim, B.-G. Park, C. S. Leem, J. Yu, T. W. Noh, C. Kim, S.-J. Oh, J.-H. Park, V. Durairaj, G. Cao, and E. Rotenberg, Phys. Rev. Lett. 101, 076402 (2008).
- [35] M. Grioni, J. F. van Acker, M. T. Czyžyk, and J. C. Fuggle, Phys. Rev. B 45, 3309 (1992).
- [36] D. T. Cromer and D. A. Liberman, Acta Crystallogr. Sect. A: Cryst. Phys. Diffr. Theor. Gen. Crystallogr. 37, 267 (1981).
- [37] G. van der Laan and B. T. Thole, Phys. Rev. Lett. 60, 1977 (1988).
- [38] M. A. Laguna-Marco, D. Haskel, N. Souza-Neto, J. C. Lang, V. V. Krishnamurthy, S. Chikara, G. Cao, and M. van Veenendaal, Phys. Rev. Lett. 105, 216407 (2010).
- [39] M. Abramchuk, O. I. Lebedev, O. Hellman, F. Bahrami, N. E. Mordvinova, J. W. Krizan, K. R. Metz, D. Broido, and F. Tafti, Inorg. Chem. 57, 12709 (2018).
- [40] I. Kimchi, J. P. Sheckelton, T. M. McQueen, and P. A. Lee, Nat. Commun. 9, 4367 (2018).
- [41] Y. S. Choi, C. H. Lee, S. Lee, S. Yoon, W. J. Lee, J. Park, A. Ali, Y. Singh, J. C. Orain, G. Kim, J. S. Rhyee, W. T. Chen, F. Chou, and K. Y. Choi, Phys. Rev. Lett. 122, 167202 (2019).